



## Communication

Graded interface engineering of 3D/2D halide perovskite solar cells through ultrathin (PEA)<sub>2</sub>PbI<sub>4</sub> nanosheetsLijie Zhu<sup>a,b</sup>, Qipeng Lu<sup>c</sup>, Chunhai Li<sup>a,b</sup>, Yue Wang<sup>a</sup>, Zhenbo Deng<sup>a,\*</sup><sup>a</sup> Key Laboratory of Luminescence and Optical Information, Ministry of Education, Beijing JiaoTong University, Beijing 100044, China<sup>b</sup> School of Instrument Science and Opto-Electronics Engineering, Beijing Information Science and Technology University, Beijing 100192, China<sup>c</sup> School of Materials Science and Engineering, University of Science and Technology Beijing, Beijing 100083, China

## ARTICLE INFO

## Article history:

Received 21 October 2020

Received in revised form 23 November 2020

Accepted 23 November 2020

Available online 5 January 2021

## Keywords:

Interface engineering

Perovskite solar cell

Two-dimensional perovskite

Hole extraction layer

Band alignment

## ABSTRACT

2D halide perovskites have emerged as promising materials because of their stability and passivation effect in perovskite solar cells (PSCs). However, the introduction of bulky organic ammonium cations from 2D halide perovskites would decrease the device performance generally compared to the traditional 3D MAPbI<sub>3</sub>. Incorporation of ultrathin 2D halide perovskite nanosheets (NSs) with 3D MAPbI<sub>3</sub> could address this issue. Herein, we report a rationally designed PSCs with dimensional graded 3D/2D MAPbI<sub>3</sub>/(PEA)<sub>2</sub>PbI<sub>4</sub> heterojunction, in which 2D (PEA)<sub>2</sub>PbI<sub>4</sub> NSs were synthesized and incorporated between 3D MAPbI<sub>3</sub> and hole-transporting layer. Besides the significantly improved stability, a notable increment in power conversion efficiency (PCE) of 20% was obtained for the 3D/2D perovskite solar cells due to the favourable band alignment among (PEA)<sub>2</sub>PbI<sub>4</sub> NSs and the other components. The graded structure of MAPbI<sub>3</sub>/(PEA)<sub>2</sub>PbI<sub>4</sub> would upshift the energy level continuously, which enhances the hole extraction efficiency thus reduces the interface charge recombination, leading to the increments of V<sub>OC</sub> from 1.04 V to 1.07 V, J<sub>SC</sub> from 21.81 mA/cm<sup>2</sup> to 23.15 mA/cm<sup>2</sup> and the fill factor from 67.89% to 74.78%, and therefore an overall PCE of 18.53%.

© 2021 Chinese Chemical Society and Institute of Materia Medica, Chinese Academy of Medical Sciences. Published by Elsevier B.V. All rights reserved.

Organic-inorganic hybrid perovskite materials have been considered as one of the most promising materials in fabricating novel optoelectronic devices such as photodetectors, light-emitting diodes, and solar cells [1]. They possess several remarkable properties, such as strong absorption coefficient, long carrier diffusion length, high ambipolar charge mobility and strong potential for solution processing [2–5]. For perovskite solar cells (PSCs), the power conversion efficiency (PCE) has been improved rapidly in recent years [6,7]. And in most of the PSCs with high PCE, the archetypal three-dimensional (3D) crystals, *i.e.*, MAPbI<sub>3</sub> and FAPbI<sub>3</sub>, are still the primary choice [8,9]. However, these 3D hybrid perovskites always show a poor tolerance to moist environment, due to the inevitable hygroscopicity and volatility of the small organic cations in their structures. Thus, the intrinsic instability of perovskite materials is still a major obstacle limiting their real applications [10,11].

Recently, it has been reported that two-dimensional (2D) perovskites showed promising long-term stability upon humidity,

heat stress, and light intensity compared to 3D perovskites, because of their hydrophobic nature of the relatively large organic cations in 2D crystal structures [12–16]. Therefore, it is a feasible strategy to incorporate the 2D perovskites with long-chain alkyl-ammonium halide into the 3D perovskites as active layer thus suppress the moisture-induced degradation [17,18]. However, directly inserting the 2D segments would change the pristine 3D structure, which severely impairs the efficient charge transport [19–21]. To overcome this problem, 2D perovskite could be employed as the capping layer on 3D crystalline films by using the spin-coating or cation exchange methods, thus forming the 3D/2D heterojunction structure [22–24]. In this structure, 2D perovskite layers have strong potential in passivation of surface-defect and grain-boundary for 3D perovskites [25–27]. Meanwhile, it has been demonstrated that the formed 3D/2D interface could improve PCE and prolong device stability [28,29]. But in the mentioned methods, it is important to find an optimal concentration of the long-chain organic molecular and proper reaction time for cation exchange. The improper concentration and reaction time may induce excessive or insufficient cation exchange, yielding poor device performance [19,22,30]. Thus, it is critical to develop a facile method to reach the optimal balance for long-term durability and

\* Corresponding author.

E-mail address: [zbdeng@bjtu.edu.cn](mailto:zbdeng@bjtu.edu.cn) (Z. Deng).

the high PCE. Meanwhile, the close contact between 3D and 2D perovskite layers is also important for the improvement of charge transporting within the PSCs.

To address these mentioned problems, herein, we rationally designed the heterojunction with graded structure in PSCs, in which the 3D perovskite material (*i.e.*, MAPbI<sub>3</sub>) and 2D perovskite material (*i.e.*, (PEA)<sub>2</sub>PbI<sub>4</sub>) were used as the active layer and capping layer, respectively. It is noteworthy that the 2D (PEA)<sub>2</sub>PbI<sub>4</sub> NSs were synthesized firstly and incorporated between 3D MAPbI<sub>3</sub> and hole-transporting material (HTM) layers to realize the band alignment thus enhance the PCE. From the characterizations, the introduced (PEA)<sub>2</sub>PbI<sub>4</sub> NSs could form 3D/2D heterostructure within the PSCs thus improve the electron blocking and hole injection characteristics at the interface between MAPbI<sub>3</sub> and HTM. And a significant increase in PCE from 15.40% to 18.53% could be achieved. Notably, the 2D (PEA)<sub>2</sub>PbI<sub>4</sub> NSs with hydrophobic property could enhance the device stability against moisture environment.

The free-standing (PEA)<sub>2</sub>PbI<sub>4</sub> NSs with ultrathin thickness were synthesized by using a facile antisolvent method, which have been reported by us previously (see Experimental details in Supporting information) [31]. Fig. 1a shows the crystal structure of the synthesized NSs. The -NH<sub>2</sub> groups from the PEA cations are bonded to the [PbI<sub>x</sub>]<sup>2-x</sup> octahedral thus assembled into the 2D structure. The transmission electron microscopy (TEM) images (Figs. 1b and c) show the morphology of the synthesized (PEA)<sub>2</sub>PbI<sub>4</sub> NSs. The NSs with rectangle shape possess the lateral size up to several hundred nanometres. The statistical data (Fig. S1b in Supporting information) analyzed from the SEM image in Fig. S1a (Supporting information) shows that the average lateral size of the (PEA)<sub>2</sub>PbI<sub>4</sub> NSs is 647.5 ± 185.0 nm. The X-ray diffraction (XRD) result (Fig. 1d) shows the periodic diffraction pattern, *i.e.*, a series of (00L) (L = 2, 4, 6, 8) reflections, which could be indexed to the interlayer spacing of (PEA)<sub>2</sub>PbI<sub>4</sub>. Meanwhile, the selected area electron diffraction (SAED) pattern (inset of Fig. 1c) demonstrated the single-crystalline nature of the (PEA)<sub>2</sub>PbI<sub>4</sub> NS. These results are consistent with our previous results [31].

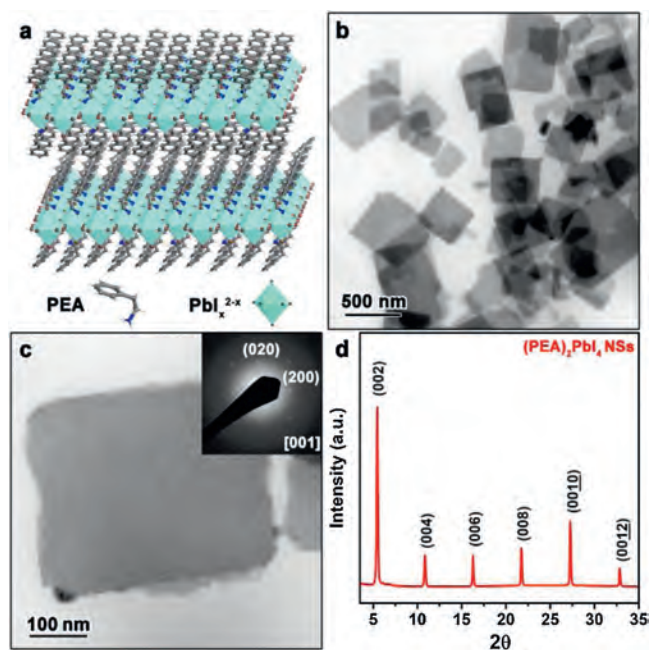


**Fig. 1.** (a) Schematic illustration of 2D structure of (PEA)<sub>2</sub>PbI<sub>4</sub> NSs. (b) TEM image of the (PEA)<sub>2</sub>PbI<sub>4</sub> NSs. (c) TEM image of the single (PEA)<sub>2</sub>PbI<sub>4</sub> NS. Inset: SAED pattern of a typical (PEA)<sub>2</sub>PbI<sub>4</sub> NS. (d) XRD pattern of the (PEA)<sub>2</sub>PbI<sub>4</sub> NSs.

To determine the bandgap of the (PEA)<sub>2</sub>PbI<sub>4</sub> NSs and MAPbI<sub>3</sub>, UV-vis absorption spectroscopy was employed, and the results are shown in Fig. S2 (Supporting information). The optical band gap ( $E_g$ ) could be calculated from the Tauc's formula. The  $E_g$  of MAPbI<sub>3</sub> and (PEA)<sub>2</sub>PbI<sub>4</sub> NSs are 1.65 and 2.23 eV, respectively. Evidently, replacing MA<sup>+</sup> with larger cations leads to an increase of bandgap [32]. Meanwhile, ultra-violet photoemission spectra (UPS, Fig. 2a) was used to investigate the energy levels of these perovskites (*i.e.*, MAPbI<sub>3</sub> and 2D (PEA)<sub>2</sub>PbI<sub>4</sub> NSs) [33,34]. The valence band maximum (VBM) level values could be calculated from Fig. 2a. And the conduction band minimum (CBM) level values, calculated by using the equation CB = VB + energy gap, are 4.07 and 3.48 eV for MAPbI<sub>3</sub> and (PEA)<sub>2</sub>PbI<sub>4</sub> NSs, respectively. All above energy levels results are summarized in Table S1 (Supporting information). From the aspect of band alignment in PSCs, the synthesized 2D (PEA)<sub>2</sub>PbI<sub>4</sub> NSs could be employed as the hole extraction layers in MAPbI<sub>3</sub>-based PSCs. The structure of fabricated device is ITO/TiO<sub>2</sub>/MAPbI<sub>3</sub>/2D (PEA)<sub>2</sub>PbI<sub>4</sub> NSs/spiro-OMeTAD/MoO<sub>3</sub>/Ag (see Methods in the Supporting information). Meanwhile, the schematic energy level diagram of each materials in the 3D/2D devices is provided in Fig. 2b. From the analyses of energy levels for different components, the VBM of (PEA)<sub>2</sub>PbI<sub>4</sub> NS is located between the VBM of MAPbI<sub>3</sub> and the highest occupied molecular orbital (HOMO) of Spiro-MeOTAD, which could provide highly effective pathways for hole transport thus reduce the interfacial charge recombination loss.

The corresponding cross-section scanning electron microscope (SEM) image of PSCs was taken to demonstrate the structure of devices, as shown in the Fig. 2c. Different from the cross-section SEM image taken from the complete device, the top-down images were aimed to observe the uniformity and continuity of the (PEA)<sub>2</sub>PbI<sub>4</sub> NSs on the 3D MAPbI<sub>3</sub> layer. Figs. 2d and e show the morphology of the 3D MAPbI<sub>3</sub> and 3D/2D MAPbI<sub>3</sub>/(PEA)<sub>2</sub>PbI<sub>4</sub> films, respectively.

Apparently, the pristine 3D film was densely packed and composed of MAPbI<sub>3</sub> crystals with grain-size around 200 nm. After spin-coating the synthesized (PEA)<sub>2</sub>PbI<sub>4</sub> NSs, the surface of MAPbI<sub>3</sub> was fully covered with the (PEA)<sub>2</sub>PbI<sub>4</sub> NSs. After fabricated the whole device, the changes in the morphology of (PEA)<sub>2</sub>PbI<sub>4</sub> NSs based devices are negligible according to the cross-section SEM image due to the introduction of thicker spiro-OMeTAD layer. Meanwhile, the X-ray diffraction (XRD) measurement was carried out to prove the presence of (PEA)<sub>2</sub>PbI<sub>4</sub> NSs on the surface of MAPbI<sub>3</sub>. Fig. 2f shows the composite films contain two sets of peaks, which could be indexed to the crystalline MAPbI<sub>3</sub> and (PEA)<sub>2</sub>PbI<sub>4</sub> NSs. After the deposition of (PEA)<sub>2</sub>PbI<sub>4</sub> NSs, the main diffraction peaks associated with the (110), (220) and (222) plane from MAPbI<sub>3</sub> show no changes. And a new set of diffraction peaks for 2D (PEA)<sub>2</sub>PbI<sub>4</sub> NSs associated with the (002) and (004) planes appeared in the patterns of composite film. Moreover, Fig. S3 (Supporting information) presents the high resolution XPS spectra for the C, N, Pb and I elements in both MAPbI<sub>3</sub> and MAPbI<sub>3</sub>/(PEA)<sub>2</sub>PbI<sub>4</sub> composite film, respectively. The XPS spectra of the MAPbI<sub>3</sub> and MAPbI<sub>3</sub>/(PEA)<sub>2</sub>PbI<sub>4</sub> films show the same peak positions and comparable intensities. The binding energy for Pb 4f<sub>5/2</sub> and Pb 4f<sub>7/2</sub> are located at 142.7 eV and 137.9 eV, and the characteristic peaks for I 3d<sub>3/2</sub> and I 3d<sub>5/2</sub> are observed at 630.4 eV and 618.9 eV, respectively.

To investigate the function of (PEA)<sub>2</sub>PbI<sub>4</sub> NSs layers in PSCs, the current density *versus* voltage (*J-V*) curves for the best PSC devices under AM 1.5 G irradiation (100 MW/cm<sup>2</sup>) are shown in Fig. 3a. The MAPbI<sub>3</sub> device as the reference device produced a PCE of 15.4%, with a  $V_{OC}$  of 1.04 V, a  $J_{SC}$  of 21.81 mA/cm<sup>2</sup>, and an FF of 67.89%. Upon the introduction of (PEA)<sub>2</sub>PbI<sub>4</sub> NSs at the interface of MAPbI<sub>3</sub> film and HTL layer (*i.e.*, spiro-OMeTAD), the photovoltaic performance improved significantly. the 3D/2D MAPbI<sub>3</sub>/(PEA)<sub>2</sub>PbI<sub>4</sub>

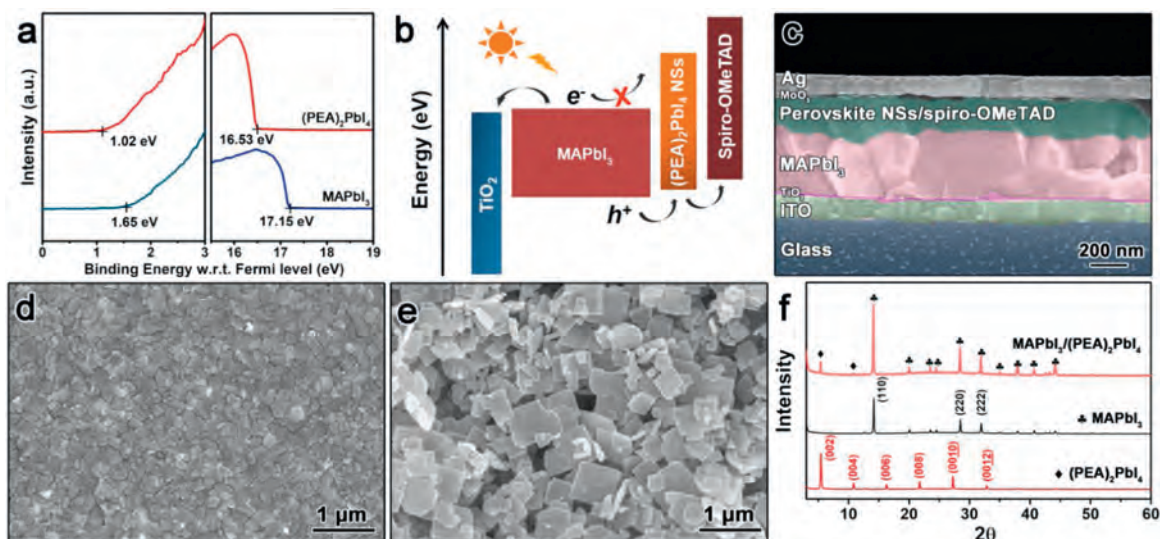


**Fig. 2.** (a) UPS spectra of MAPbI<sub>3</sub> and (PEA)<sub>2</sub>PbI<sub>4</sub> NS films on ITO glass as substrate. (b) Schematic energy level diagram of the 3D/2D MAPbI<sub>3</sub>/(PEA)<sub>2</sub>PbI<sub>4</sub> PSCs. (c) Cross-sectional SEM image of a typical MAPbI<sub>3</sub> PSC with incorporation of 2D (PEA)<sub>2</sub>PbI<sub>4</sub> NSs. (d) Top-view SEM image of MAPbI<sub>3</sub> film. (e) Top-view SEM image of 2D (PEA)<sub>2</sub>PbI<sub>4</sub> NSs covered on the MAPbI<sub>3</sub> film. (f) XRD patterns of the (PEA)<sub>2</sub>PbI<sub>4</sub> NS, MAPbI<sub>3</sub> and MAPbI<sub>3</sub>/(PEA)<sub>2</sub>PbI<sub>4</sub> composite films, respectively.

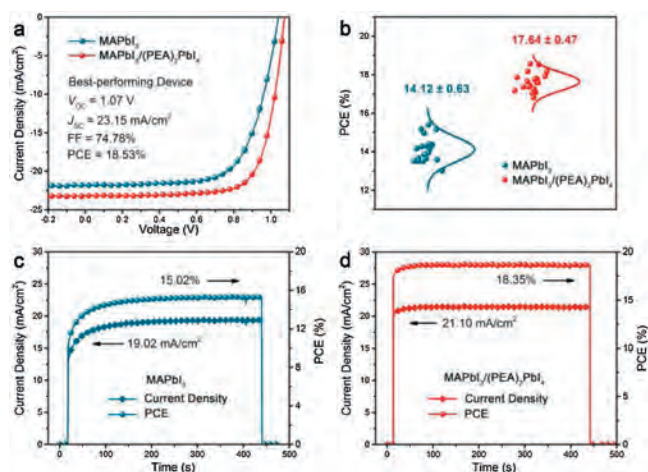


**Fig. 3.** (a) *J-V* characteristics of the best performing devices based on MAPbI<sub>3</sub> and MAPbI<sub>3</sub>/(PEA)<sub>2</sub>PbI<sub>4</sub> perovskite films. (b) Statistics of the PCE distribution for the fabricated MAPbI<sub>3</sub> and MAPbI<sub>3</sub>/(PEA)<sub>2</sub>PbI<sub>4</sub> PSCs (20 devices). (c) Steady-state photocurrent density of MAPbI<sub>3</sub> PSCs at the maximum power point (0.79 V). (d) Steady-state photocurrent density of MAPbI<sub>3</sub>/(PEA)<sub>2</sub>PbI<sub>4</sub> PSCs at the maximum power point (0.87 V).

device produced a  $V_{OC}$  of 1.07 V, a  $J_{SC}$  of 23.15 mA/cm<sup>2</sup>, and an FF of 74.78%, corresponding to a PCE of 18.53%. The significant improved  $J_{SC}$  and FF as well as the slightly increased  $V_{OC}$  play the key roles in the enhancement of PCE. To test the reproducibility, we fabricated twenty samples for each type of PSCs and evaluated their photovoltaic performance. Fig. 3b and Fig. S4 (Supporting information) show the statistics of detailed parameters for these two types of devices. The PCEs of MAPbI<sub>3</sub>/(PEA)<sub>2</sub>PbI<sub>4</sub> devices were distributed in a relatively narrow range, indicated their excellent reproducibility. The average photovoltaic parameters could be found in the Table S2 (Supporting information). The average PCEs of MAPbI<sub>3</sub> and MAPbI<sub>3</sub>/(PEA)<sub>2</sub>PbI<sub>4</sub> PSCs obtained in our work were 14.12 ± 0.63% and 17.64 ± 0.47%, respectively. These results are consistent with that of the best parameters of two kinds of devices. And the performance is comparable to the best perovskite solar

cells with 3D/perovskite nanomaterial heterostructures (Table S3 in Supporting information).

Photocurrent hysteresis is another important factor for the PSCs. In Fig. S5 and Table S4 (Supporting information), the MAPbI<sub>3</sub> PSCs exhibited an obvious photocurrent hysteresis with PCEs of 15.40% and 7.58% under a reverse (from forward bias to short circuit) and forward scan (from short circuit to forward bias), respectively. Hence, the hysteresis factor could be quantified by using the following equation:

$$\text{Hysteresis factor} = (\text{PCE}_{\text{reverse}} - \text{PCE}_{\text{forward}}) / \text{PCE}_{\text{reverse}}$$

Compared with the high hysteresis factor from MAPbI<sub>3</sub> PSCs (*i.e.*, 50.8%), the MAPbI<sub>3</sub>/(PEA)<sub>2</sub>PbI<sub>4</sub> PSCs exhibited a decreased hysteresis factor of 43.7%. The current peak could be observed from the forward bias region for the reverse scans, indicating a typical signal for a diode. These results clearly demonstrated it requires a longer time to reach to the stable operation [32]. According to the literature, the deteriorative degrade of hysteresis is strongly dependent on the device structure. At the same scan rate, the MAPbI<sub>3</sub> device with the planar structure shows a more obvious hysteresis [35]. To further study the hysteresis, we also measured the steady-state photocurrent and PCE under the maximum power point over 400 s. According to the results from the Fig. 3c and Table S5 (Supporting information), the MAPbI<sub>3</sub> PSCs show a stable photocurrent of 19.02 mA/cm<sup>2</sup> when the bias voltage is 0.79 V, and generate a PCE of 15.02% which is consistent with the PCE value calculated from the *J-V* measurements. In contrast, the PCE of MAPbI<sub>3</sub>/(PEA)<sub>2</sub>PbI<sub>4</sub> PSCs rapidly reached to a stable value of 18.35% at bias voltage of 0.87 V, which is close to the best PCE value of 18.53% (Fig. 3d, Table S5). Compared to the MAPbI<sub>3</sub> PSCs, both photocurrent and PCE of MAPbI<sub>3</sub>/(PEA)<sub>2</sub>PbI<sub>4</sub> PSCs exhibited much faster response, which should be attributed to the less ionic migration, optimal graded interface, and/or synergistic of these two factors. Moreover, the faster stabilizing rate and higher stable PCE also demonstrated the less defects in the 3D/2D MAPbI<sub>3</sub>/(PEA)<sub>2</sub>PbI<sub>4</sub> perovskite film, which is also help for the decrease of charge recombination and alleviation of hysteresis.

We also analysed the absorption and photoluminescence spectra of these two films (*i.e.*, MAPbI<sub>3</sub> and MAPbI<sub>3</sub>/(PEA)<sub>2</sub>PbI<sub>4</sub>) to get better understanding about the generation and recombination of electron-hole pairs. As shown in Fig. 4a, the strong

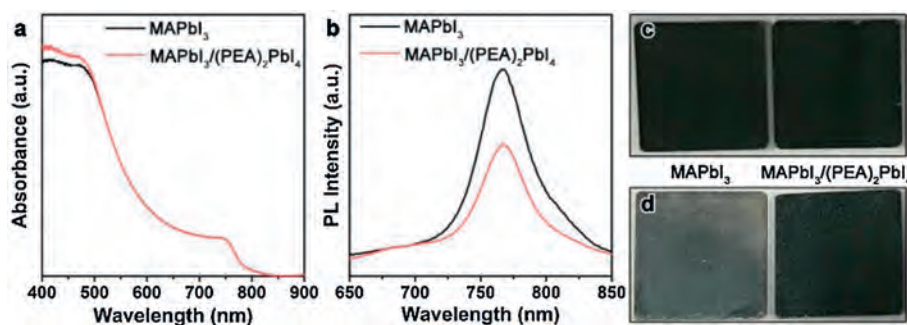


**Fig. 4.** (a) UV-vis absorption spectrum of MAPbI<sub>3</sub> and MAPbI<sub>3</sub>/(PEA)<sub>2</sub>PbI<sub>4</sub> films. (b) Steady-state photoluminescence curves for MAPbI<sub>3</sub> and MAPbI<sub>3</sub>/(PEA)<sub>2</sub>PbI<sub>4</sub> films detected from the glass side in the wavelength range of 670–850 nm. Images of (c) original perovskite film and (d) perovskite film after exposing in an ambient environment at 30 °C and with 90% ± 5% relative humidity for 5 h. Left: MAPbI<sub>3</sub> film, right: MAPbI<sub>3</sub>/(PEA)<sub>2</sub>PbI<sub>4</sub> film.

absorption of these films is mainly come from the active layer, *i.e.*, MAPbI<sub>3</sub>. Due to the thin thickness of the (PEA)<sub>2</sub>PbI<sub>4</sub>, there is a slight enhancement for the absorption of the (PEA)<sub>2</sub>PbI<sub>4</sub> below 500 nm. Meanwhile, because of small amount of (PEA)<sub>2</sub>PbI<sub>4</sub> NSs on the active layer, theoretically, the light absorption properties of (PEA)<sub>2</sub>PbI<sub>4</sub> NSs cannot improve the light harvesting strongly. Therefore, the difference in PCE should be ascribed to the graded interface introduced by the (PEA)<sub>2</sub>PbI<sub>4</sub> NSs on MAPbI<sub>3</sub>. To further investigate the interaction between the MAPbI<sub>3</sub> and (PEA)<sub>2</sub>PbI<sub>4</sub> NSs, photoluminescence measurements were employed. From the Fig. 4b, the emission of both samples is centered at 770 nm, which is attribute to exciton recombination and luminescence of MAPbI<sub>3</sub>. However, compared to the MAPbI<sub>3</sub>, the decreased photoluminescence intensity indicates a faster electron-hole separation followed by the hole extraction with the introduced (PEA)<sub>2</sub>PbI<sub>4</sub> NSs on MAPbI<sub>3</sub>. According to the proposed mechanism from Fig. 2b, the photo generated holes in the MAPbI<sub>3</sub> film could firstly transfer to the (PEA)<sub>2</sub>PbI<sub>4</sub> NSs then to the HTM layer, which is propitious to the improvement of PCE of PSCs.

Besides the improved photovoltaic efficiency, another major concern is the durability of PSCs for real application, especially under moisture conditions. To directly evaluate their moisture stability, we tested the stability of the MAPbI<sub>3</sub> film (left image in Fig. 4c) and MAPbI<sub>3</sub>/(PEA)<sub>2</sub>PbI<sub>4</sub> composite film (right image in Fig. 4c) without any encapsulation under the ambient conditions at 30 °C and with the relative humidity of 90% ± 5%. After 5 h, the pure MAPbI<sub>3</sub> film degraded dramatically, as shown in left image in Fig. 4d. However, there were no obvious colour changes for MAPbI<sub>3</sub>/(PEA)<sub>2</sub>PbI<sub>4</sub> composite film (right image in Fig. 4c), indicating the 2D (PEA)<sub>2</sub>PbI<sub>4</sub> NSs could provide sufficient protection for MAPbI<sub>3</sub> films from the high moisture environment.

We fabricated PSCs based on 3D/2D MAPbI<sub>3</sub>/(PEA)<sub>2</sub>PbI<sub>4</sub> with dimensional graded heterojunction, which exhibited improved PCE and stability under moisture conditions. Comprehensive characterizations were carried out to investigate the effect of 2D (PEA)<sub>2</sub>PbI<sub>4</sub> NSs on the performance of PSCs. It is demonstrated that the graded structure of MAPbI<sub>3</sub>/(PEA)<sub>2</sub>PbI<sub>4</sub> could upshift the energy level, thus enhancing the hole extraction efficiency and decreasing the interface charge recombination. With the assistance of (PEA)<sub>2</sub>PbI<sub>4</sub> NSs, the improved interfacial characteristics lead to an increasement in PCE with enhanced  $V_{OC}$ ,  $J_{SC}$  and FF.

#### Declaration of competing interest

The authors report no declarations of interest.

#### Acknowledgments

The authors acknowledge the financial support of the National Natural Science Foundation of China (No. 61775011), and the Supplementary and Supportive Project for Teachers at Beijing Information Science and Technology University (2019–2021) (No. 5029011103).

#### Appendix A. Supplementary data

Supplementary material related to this article can be found, in the online version, at doi:<https://doi.org/10.1016/j.ccl.2020.12.052>.

#### References

- [1] Z. Wei, Y. Zhao, J. Jiang, et al., *Chin. Chem. Lett.* 31 (2020) 3055–3064.
- [2] S.D. Stranks, G.E. Eperon, G. Grancini, et al., *Science* 342 (2013) 341–344.
- [3] G. Xing, N. Mathews, S. Sun, et al., *Science* 342 (2013) 344–347.
- [4] Q. Dong, Y. Fang, Y. Shao, et al., *Science* 347 (2015) 967–970.
- [5] T.M. Brenner, D.A. Egger, L. Kronik, et al., *Nat. Rev. Mater.* 1 (2016) 15007.
- [6] X. Sun, D. Zhao, Z.a. Li, *Chin. Chem. Lett.* 29 (2018) 219–231.
- [7] Y. Yang, N.D. Pham, D. Yao, et al., *Chin. Chem. Lett.* 29 (2018) 1242–1250.
- [8] W.S. Yang, B.W. Park, E.H. Jung, et al., *Science* 356 (2017) 1376–1379.
- [9] H. Zai, C. Zhu, H. Xie, et al., *ACS Energy Lett.* 3 (2018) 30–38.
- [10] Y. Rong, Y. Hu, A. Mei, et al., *Science* 361 (2018) eaat8235.
- [11] T. Leijtens, K. Bush, R. Cheacharoen, et al., *J. Mater. Chem. A* 5 (2017) 11483–11500.
- [12] J. Yan, W. Qiu, G. Wu, et al., *J. Mater. Chem. A* 6 (2018) 11063–11077.
- [13] I.C. Smith, E.T. Hoke, D. Solis-Ibarra, et al., *Angew. Chem.* 126 (2014) 11414–11417.
- [14] F. Xu, T. Zhang, G. Li, Y. Zhao, *J. Mater. Chem. A* 5 (2017) 11450–11461.
- [15] S. Yang, W. Niu, A.L. Wang, et al., *Angew. Chem. Int. Ed.* 56 (2017) 4252–4255.
- [16] S. Ahmad, X. Guo, *Chin. Chem. Lett.* 29 (2018) 657–663.
- [17] J.W. Lee, Z. Dai, T.H. Han, et al., *Nat. Commun.* 9 (2018) 3021.
- [18] Z. Wang, Q. Lin, F.P. Chmiel, et al., *Nat. Energy* 2 (2017) 17135.
- [19] D.S. Lee, J.S. Yun, J. Kim, et al., *ACS Energy Lett.* 3 (2018) 647–654.
- [20] C.M.M. Soe, W. Nie, C.C. Stoumpos, et al., *Adv. Energy Mater.* 8 (2018) 1700979.
- [21] B.E. Cohen, M. Wierzbowska, L. Etgar, *Adv. Funct. Mater.* 27 (2017) 1604733.
- [22] P. Chen, Y. Bai, S. Wang, et al., *Adv. Funct. Mater.* 28 (2018) 1706923.
- [23] Y. Bai, S. Xiao, C. Hu, et al., *Adv. Energy Mater.* 7 (2017) 1701038.
- [24] M. Tai, Y. Zhou, X. Yin, et al., *J. Mater. Chem. A* 7 (2019) 22675–22682.
- [25] Q. Jiang, Y. Zhao, X. Zhang, et al., *Nat. Photonics* 13 (2019) 460–466.
- [26] E.A. Alharbi, A.Y. Alyamani, D.J. Kubicki, et al., *Nat. Commun.* 10 (2019) 3008.
- [27] X. Xu, Z. Li, L. Zhu, et al., *J. Mater. Chem. A* 7 (2019) 1341–1348.
- [28] T. Zhang, M. Long, M. Qin, et al., *Joule* 2 (2018) 2706–2721.
- [29] G. Liu, H. Zheng, X. Xu, et al., *J. Mater. Chem. A* 6 (2018) 18067–18074.
- [30] Y. Cho, A.M. Soufiani, J.S. Yun, et al., *Adv. Energy Mater.* 8 (2018) 1703392.
- [31] L. Zhu, H. Zhang, Q. Lu, et al., *J. Mater. Chem. C* 6 (2018) 3945–3950.
- [32] C. Li, J. Wei, M. Sato, et al., *ACS Appl. Mater. Interfaces* 8 (2016) 11526–11531.
- [33] L. Lv, Q. Lu, Y. Ning, et al., *Chem. Mater.* 27 (2015) 44–52.
- [34] H.Y. Zhang, R. Li, W.W. Liu, et al., *Int. J. Miner. Metall. Mater.* 26 (2019) 387–403.
- [35] H.S. Kim, N.G. Park, *J. Phys. Chem. Lett.* 5 (2014) 2927–2934.